

Article

ARGET-ATRP-Mediated Grafting of Bifunctional Polymers onto Silica Nanoparticles Fillers for Boosting the Performance of High-Capacity All-Solid-State Lithium–Sulfur Batteries with Polymer Solid Electrolytes

Liang Wang ¹, Junyue Huang ¹, Yujian Shen ¹, Mengqi Ma ¹, Wenhong Ruan ^{1,2,*} and Mingqiu Zhang ^{1,2}

¹ Key Laboratory for Polymeric Composite and Functional Materials of Ministry of Education, GD HPPC Lab, School of Chemistry, Sun Yat-sen University, Guangzhou 510275, China; wangln57@mail2.sysu.edu.cn (L.W.); huangjy329@mail2.sysu.edu.cn (J.H.); shenyj7@mail2.sysu.edu.cn (Y.S.); mamq6@mail2.sysu.edu.cn (M.M.); ceszmq@mail.sysu.edu.cn (M.Z.)

² Guangdong Provincial Laboratory of Chemistry and Fine Chemical Engineering Jieyang Center, Jieyang 515200, China

* Correspondence: cesrwh@mail.sysu.edu.cn; Tel.: +86-020-84114008

Abstract: The shuttle effect in lithium–sulfur batteries, which leads to rapid capacity decay, can be effectively suppressed by solid polymer electrolytes. However, the lithium-ion conductivity of polyethylene oxide-based solid electrolytes is relatively low, resulting in low reversible capacity and poor cycling stability of the batteries. In this study, we employed the activator generated through electron transfer atom transfer radical polymerization to graft modify the surface of silica nanoparticles with a bifunctional monomer, 2-acrylamide-2-methylpropanesulfonate, which possesses sulfonic acid groups with low dissociation energy for facilitating Li⁺ migration and transfer, as well as amide groups capable of forming hydrogen bonds with polyethylene oxide chains. Subsequently, the modified nanoparticles were blended with polyethylene oxide to prepare a solid polymer electrolyte with low crystallinity and high ion conductivity. The resulting electrolyte demonstrated excellent and stable electrochemical performance, with a discharge-specific capacity maintained at 875.2 mAh g^{−1} after 200 cycles.

Keywords: ARGET-ATRP; silica nanoparticles; lithium–sulfur batteries; polymer solid electrolytes



Citation: Wang, L.; Huang, J.; Shen, Y.; Ma, M.; Ruan, W.; Zhang, M.

ARGET-ATRP-Mediated Grafting of Bifunctional Polymers onto Silica Nanoparticles Fillers for Boosting the Performance of High-Capacity All-Solid-State Lithium–Sulfur Batteries with Polymer Solid Electrolytes.

Polymers **2024**, *16*, 1128. <https://doi.org/10.3390/polym16081128>

Academic Editor: Wei-Ren Liu

Received: 5 March 2024

Revised: 13 April 2024

Accepted: 15 April 2024

Published: 17 April 2024



Copyright: © 2024 by the authors. Licensee MDPI, Basel, Switzerland. This article is an open access article distributed under the terms and conditions of the Creative Commons Attribution (CC BY) license (<https://creativecommons.org/licenses/by/4.0/>).

1. Introduction

With the continuous growth in global energy demand, lithium-ion batteries (LIBs) with high energy density and long cycling capability have experienced widespread development, playing an increasingly significant role in the global energy system [1–3]. The remarkable specific capacity (1672 mAh g^{−1}) and cost-effectiveness have garnered extensive attention for sulfur cathodes in the field of lithium batteries [4]. Among them, lithium–sulfur (Li-S) batteries, which are compatible with the coveted lithium metal as the anode, represent one of the most extensively researched types of LIBs [5–8].

However, in conventional liquid-state LIB systems, the favorable solubility of lithium polysulfides (LiPSs) generated at the cathode during battery cycling leads to continuous loss of active materials in the cathode [8–12]. These soluble LiPSs (Li₂S_x, 4 < x < 8) migrate to the anode side with the electrolyte, a phenomenon known as the “shuttle effect”, where they react with the lithium metal, forming insoluble Li₂S₂ and Li₂S, which subsequently deposit on the lithium metal surface [13–15]. This seemingly promising cathode material simultaneously gives rise to the aforementioned issues on both the cathode and anode, resulting in rapid capacity decay of Li-S batteries. The development of all-solid-state Li-S batteries holds tremendous potential for the commercialization of Li-S battery technology [16–20]. Solid polymer electrolytes (SPEs) can play a crucial role by acting as physical

barriers, effectively controlling the dissolution of LiPSs from the cathode and mitigating their negative impact on the anode [18,21–24]. Additionally, SPEs offer a range of advantages, such as preventing electrolyte leakage, enabling high energy density, and enhancing safety [24–26]. In the realm of SPEs, blends of high molecular weight polyethylene oxide (PEO) and its derivatives with lithium salts have gained considerable attention [27–31]. This stems from the favorable attributes of PEO, including excellent mechanical properties, high solubility with lithium salts, and favorable chemical stability towards lithium metal [32]. The mechanism by which PEO-based polymer solid electrolytes facilitate Li⁺ transport is through the coordination of Li⁺ ions, dissociated from lithium salts, with ether oxygen atoms along the PEO polymer chains. The migration and transfer of Li⁺ ions are driven by the segmental motion of the PEO polymer chains [33,34]. However, it should be noted that PEO belongs to the category of crystalline polymers, exhibiting a relatively high degree of crystallinity at lower temperatures. This characteristic hinders the effective conduction of Li⁺ ions through the crystalline regions of the PEO polymer chains, resulting in low lithium-ion conductivity (approximately 10⁻⁷ S cm⁻¹) [31]. Consequently, batteries utilizing PEO-based solid electrolytes may exhibit limited reversible capacity and suboptimal cycling stability [35–37].

The incorporation of diverse nanostructured inorganic fillers with varying surface properties into the polymer matrix of PEO to form composite SPEs represents a promising avenue to mitigate its crystallinity and enhance the performance of SPEs [38–40]. For instance, the crystallinity of PEO could be reduced by introducing Al₂O₃ or SiO₂ fillers into the polymer matrix [41–46]. This approach effectively increased the number of free polymer segments, thereby accelerating the segmental motion of the polymer chains and ultimately leading to enhanced lithium-ion conductivity.

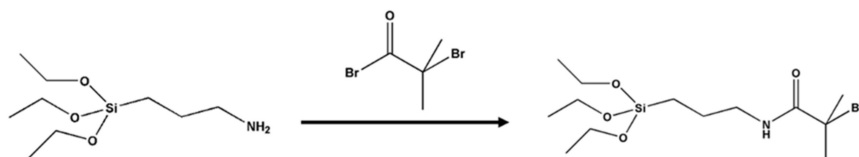
In our previous investigations, we observed the tendency of inorganic fillers with abundant polar functional groups to aggregate when incorporated into crystalline polymer matrices for modification [47]. Such poor compatibility hampers the efficiency of filler-mediated polymer modification, particularly when the filler itself is inert and lacks inherent Li⁺ conductivity. To address this challenge, surface modification of inorganic fillers has emerged as a viable approach. Motivated by this concept, we employed cost-effective and readily available silica nanoparticles (SiO₂ Nps), a typical inert filler, and employed the activators regenerated by the electron transfer atom transfer radical polymerization (ARGET-ATRP) technique to graft a bifunctional monomer lithium 2-acrylamide-2-methylpropanesulfonate (AMPSLi) onto the filler surface (SiO₂-g-PAMPSLi). This monomer possesses sulfonic acid moieties with low dissociation energy for facilitating Li⁺ migration and transfer, as well as amide groups capable of forming hydrogen bonds with PEO polymer chains. Subsequently, the modified filler was blended with PEO to fabricate SPEs with reduced crystallinity and enhanced ion conductivity.

2. Materials and Methods

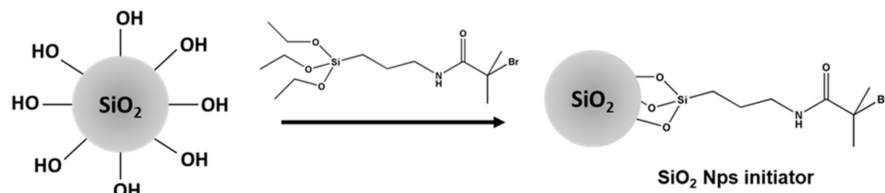
2.1. Preparation of SiO₂-g-PAMPSLi

Firstly, SiO₂ NPs were obtained by using a modified Stöber method and activated by hydrogen peroxide and concentrated sulfuric acid [48]. Then, a certain amount of 2-bromo-2-methylpropanoyl bromide, 3-aminopropyltriethoxysilane, and triethylamine were mixed to produce the siloxane pre-initiator. Under anhydrous and anaerobic conditions, SiO₂ NPs and siloxane pre-initiator reactions formed the SiO₂ Nps initiator. Then, with the initiator and AMPSLi added, the SiO₂-g-PAMPSLi nanoparticle was successfully obtained through ARGET-ATRP. The concrete process of synthesis is shown in the Supplementary Materials as well as Figure 1.

Synthesis of the pre-initiator



Synthesis of SiO₂ Nps initiator



Synthesis of SiO₂-g-PAMPSLi

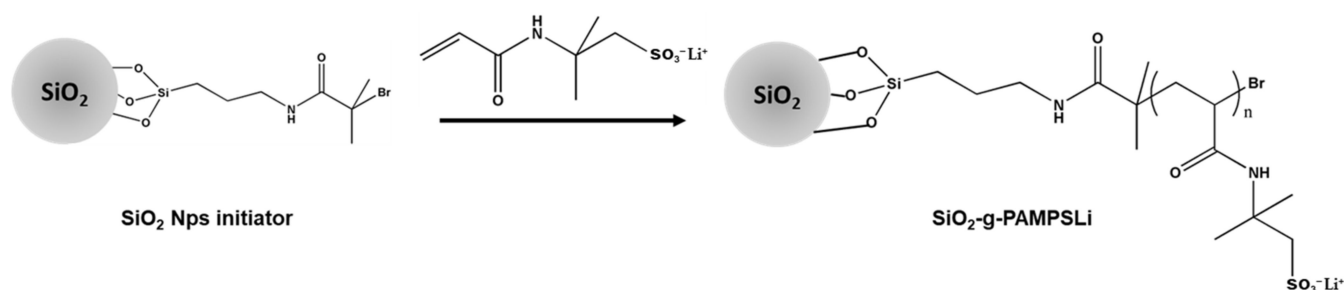


Figure 1. Preparation of SiO₂-g-PAMPSLi.

2.2. Preparation of SiO₂-g-PAMPSLi@PEO-Based Polymer Composite Solid Electrolytes

This experiment uses a solution pouring method to prepare solid electrolytes, with the specific steps as follows: (1) dissolve a certain amount of LiClO₄ in 10 mL acetonitrile according to the EO/Li⁺ ratio [49]; (2) add a certain amount of inorganic solid powder to the above solution and sonicate for 15 min to disperse; (3) add 0.88 g of polyethylene oxide (PEO) and a certain amount of SiO₂-g-PAMPSLi to the above dispersion and stir at room temperature for 24 h; then (4) pour the solution into a PTFE mold with length, width, and height of 50 mm × 50 mm × 3 mm. First, let the solvent evaporate naturally under a fume hood. Then, remove the solvent on a 40 °C hot bench and dry it in a 40 °C vacuum oven for 24 h. (5) Lastly, cut the dried solid electrolyte film into circular slices with a diameter of 16 mm using a slicer for later use.

2.3. Preparation of Carbon Sulfur Composite Cathode Materials

This experiment used an in-situ loading method to load sulfur onto Super P-activated carbon to prepare active materials. The specific steps are as follows: (1) dissolve and disperse 3 g sodium thiosulfate pentahydrate and 0.15 g Super P-activated carbon in 10 mL deionized water, stir for 15 min; (2) dissolve 2.37 g of concentrated hydrochloric acid in 23.7 mL of deionized water and slowly add it to the above solution through a constant pressure drip funnel under magnetic stirring; (3) react at room temperature for 12 h; (4) solid and liquid are separated by suction filtration, and the filter residue is washed with deionized water until the filtrate is neutral. It is then dried in a vacuum oven at 60 °C for 24 h before being set aside.

2.4. Preparation of Cathodes and Lithium–Sulfur Batteries

This experiment uses the scraping coating method to prepare the cathode of lithium–sulfur batteries. The specific steps are as follows: (1) grind and mix 0.8 g of carbon–sulfur composite material, 0.1 g of acetylene black, and 0.1 g of polyvinylidene fluoride (in a

mass ratio of 8:1:1) evenly in an agate mortar; (2) add the mixed powder to 5 mL of N-methylpyrrolidone and stir at room temperature for 12 h to obtain a viscous cathode slurry; (3) use a four-sided scraper to coat the cathode slurry onto the carbon coated aluminum foil, and dry it in a 60 °C blast oven for 12 h to remove solvents; (4) cut the carbon-coated aluminum foil coated with cathode material and dried into circular pieces with a diameter of 12 mm using a slicer, and store them in a glove box filled with argon gas atmosphere for later use.

2.5. Electrochemical Measurements

The solid electrolytes, cathodes, and lithium metal were assembled into the CR2032 button battery in a glove box filled with argon gas. The electrochemical stability window was tested by linear sweep voltammetry (LSV) measurement under a scan rate of 5 mV s⁻¹, from 2.0 to 6.0 V (vs. Li/Li⁺) in an electrochemical workstation (CHI760E, CH Instrument, Shanghai, China). The cyclic voltammetry (CV) was carried out at a scan rate of 0.1 mV s⁻¹ between 1.6 and 2.8 V to characterize the redox reaction and reversibility. The electrochemical cycling performance of the coin cells was tested within a voltage window of 1.6–2.8 V using a battery test system (CT2001A, LAND, Wuhan, China).

3. Results

Characterization of the synthesized pre-initiator was performed by dissolving it in deuterated chloroform and analyzing its chemical structure using nuclear magnetic resonance (NMR) spectroscopy. Figure S1 presents the proton NMR spectrum of the pre-initiator. From the spectrum, it can be observed that the absorption peaks at 1.21 ppm and 3.97 ppm correspond to the methyl and methylene protons on the ethoxy groups, respectively. The peaks at 0.63 ppm, 1.61 ppm, and 3.26 ppm correspond to the three methylene protons on the original amino propyl group. The peak at 6.89 ppm corresponds to the hydrogen atom in the amide group of the pre-initiator, while the peak at 1.98 ppm corresponds to the two methyl protons on the α -carbon atom connected to the carbonyl group. The ratios of the peak areas of all characteristic peaks are in complete agreement with the proportions of hydrogen atoms in the chemical structure, indicating the successful synthesis of the pre-initiator.

In order to investigate the morphological structure of SiO₂-g-PAMPSLi, scanning electron microscopy (SEM) and transmission electron microscopy (TEM) were employed for characterization. As shown in Figure S2, the surface of SiO₂ Nps particles appears smooth and uniform. However, in Figure S3, the SiO₂ Nps initiator exhibits the presence of adhered substances, indicating the successful grafting of the pre-initiator onto the surface of SiO₂ Nps. After the ARGET-ATRP polymerization reaction, Figure 2A clearly reveals that the surface of SiO₂ particles is no longer smooth, exhibiting noticeable adhered substances and agglomeration between particles. This phenomenon suggests the successful polymerization of AMPSLi monomers on the surface of SiO₂ particles, forming a polymer layer that encapsulates the SiO₂ particles and leads to interparticle adhesion. Elemental mapping analysis using energy-dispersive X-ray spectroscopy (EDS) confirms the presence of nitrogen (N) and sulfur (S) elements on the surface of SiO₂-g-PAMPSLi particles, which are exclusive to the AMPSLi monomers. This observation further confirms the successful surface modification of SiO₂ Nps. Moreover, the TEM image in Figure 2B reveals that SiO₂-g-PAMPSLi nanoparticles possess a core-shell structure, with the SiO₂ core and a PAMPSLi polymer shell formed by the polymerization of AMPSLi monomers. Infrared spectroscopy was performed on SiO₂ Nps, SiO₂ Nps initiator, and SiO₂-g-PAMPSLi, as shown in Figure 2C. For SiO₂ Nps, the strong absorption peak at 1100 cm⁻¹ corresponds to the stretching vibration of Si-O-Si bonds, while the peak at 3300 cm⁻¹ corresponds to the stretching vibration of hydroxyl groups (O-H) on the surface of SiO₂ Nps. For the SiO₂ Nps initiator, the peak at 3400 cm⁻¹ corresponds to the stretching vibration of N-H bonds on the amine group, the peak at 2925 cm⁻¹ corresponds to the stretching vibration of saturated C-H bonds, and the peak at 1620 cm⁻¹ corresponds to the stretching

vibration of C=O double bonds on the carbonyl group. These three characteristic peaks correspond to the functional groups present in the pre-initiator, and the peaks at 1465 cm^{-1} and 1402 cm^{-1} correspond to the antisymmetric and symmetric deformation vibrations of the methyl groups on the pre-initiator, respectively, indicating the successful grafting of the pre-initiator onto the surface of SiO_2 Nps to form the SiO_2 Nps initiator. For SiO_2 -g-PAMPSLi, the monomer AMPSPLi contains carbonyl, amine, and methyl groups. From the infrared spectrum, it can be observed that the intensities of the characteristic peaks corresponding to these three groups are enhanced. Additionally, the absorption peaks around 1070 cm^{-1} and 1193 cm^{-1} (overlapping with the stretching vibration peak of Si-O-Si bonds) as well as the peak at 630 cm^{-1} correspond to the antisymmetric and symmetric deformation vibrations and stretching vibration of S-O bonds on the sulfonic acid group, respectively. This further confirms the successful polymerization and grafting of AMPSPLi monomers on the surface of SiO_2 Nps, forming SiO_2 -g-PAMPSLi. Figure 2D presents the thermogravimetric analysis (TGA) curves of SiO_2 Nps, the SiO_2 Nps initiator, and SiO_2 -g-PAMPSLi. A notable observation is the 7% higher weight loss in the SiO_2 Nps initiator compared to SiO_2 Nps, confirming the successful bonding of the organic component to the surface of SiO_2 Nps and the successful synthesis of the SiO_2 initiator. Furthermore, a distinct weight loss is evident in SiO_2 -g-PAMPSLi beginning at $210\text{ }^\circ\text{C}$, indicative of the polymer grafting on the surface of SiO_2 Nps. This finding allows for the calculation of the mass fraction of the grafted polymer PAMPSLi on the SiO_2 Nps surface, estimated to be approximately 64.56%.

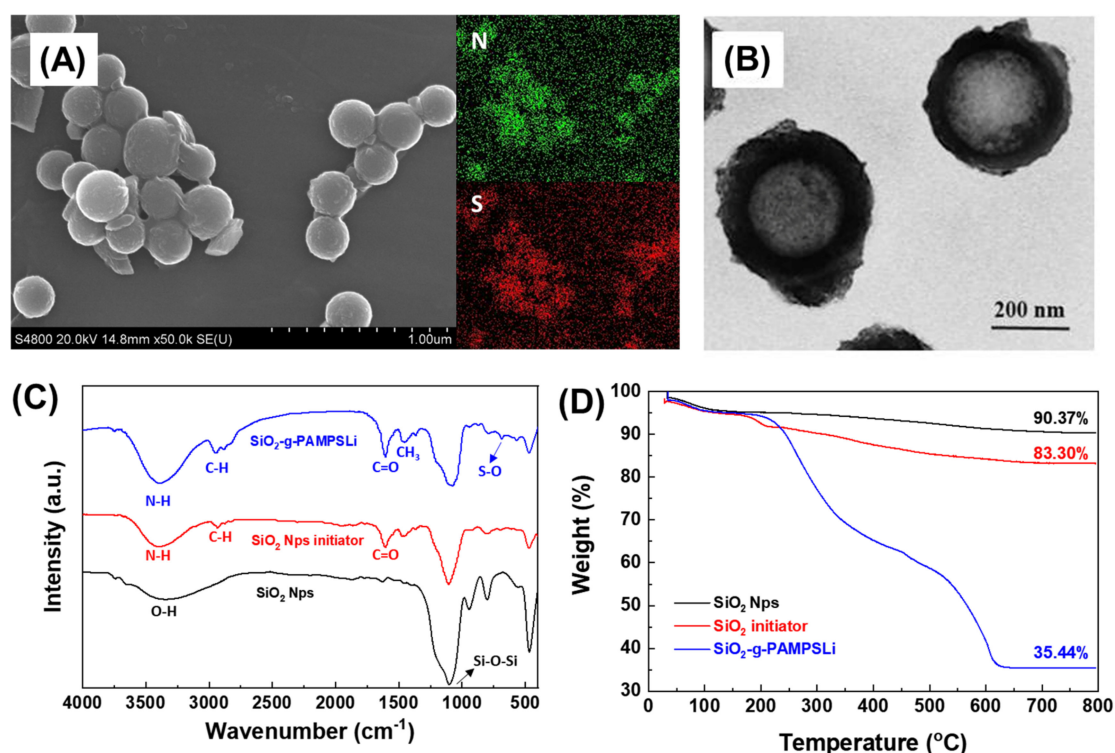


Figure 2. (A) SEM and corresponding EDS element scanning profiles and (B) TEM images of SiO_2 -g-PAMPSLi; (C) infrared spectra and (D) thermogravimetric curves of SiO_2 Nps, SiO_2 Nps initiator, and SiO_2 -g-PAMPSLi.

Composite SPEs were prepared by incorporating SiO_2 Nps and SiO_2 -g-PAMPSLi into PEO (SiO_2 @PEO and SiO_2 -g-PAMPSLi@PEO). The morphology of the two composites was examined using SEM (Figure S3). In comparison to SiO_2 @PEO, SiO_2 -g-PAMPSLi@PEO exhibited a more uniform dispersion of fillers. Even at a high loading of 20 wt%, the SiO_2 -g-PAMPSLi particles did not aggregate. This can be attributed to the presence of the PAMPSLi polymer layer, which effectively isolates the inorganic SiO_2 particles, preventing

their agglomeration. Furthermore, the polymer layer demonstrates excellent organic–organic compatibility with the PEO matrix, facilitating the homogeneous dispersion of SiO₂-g-PAMPSLi particles within the PEO matrix. However, at a loading of 25 wt%, SEM images revealed the occurrence of particle aggregation in SiO₂-g-PAMPSLi@PEO.

To investigate the influence of nanoparticles on the crystallization behavior of PEO, X-ray diffraction (XRD) and differential scanning calorimetry (DSC) characterization was performed on SPEs with different contents of SiO₂ (Figure 3A,C) and SiO₂-g-PAMPSLi (Figure 3B,D). The melting temperatures, enthalpies of fusion, and crystallinity of all substances in the DSC curves are summarized in Tables S1 and S2. The crystallinity of polymer PEO was calculated using the following equation.

$$\chi_c = \frac{\Delta H_m}{\Delta H_{PEO} \cdot f_{PEO}} \times 100\%$$

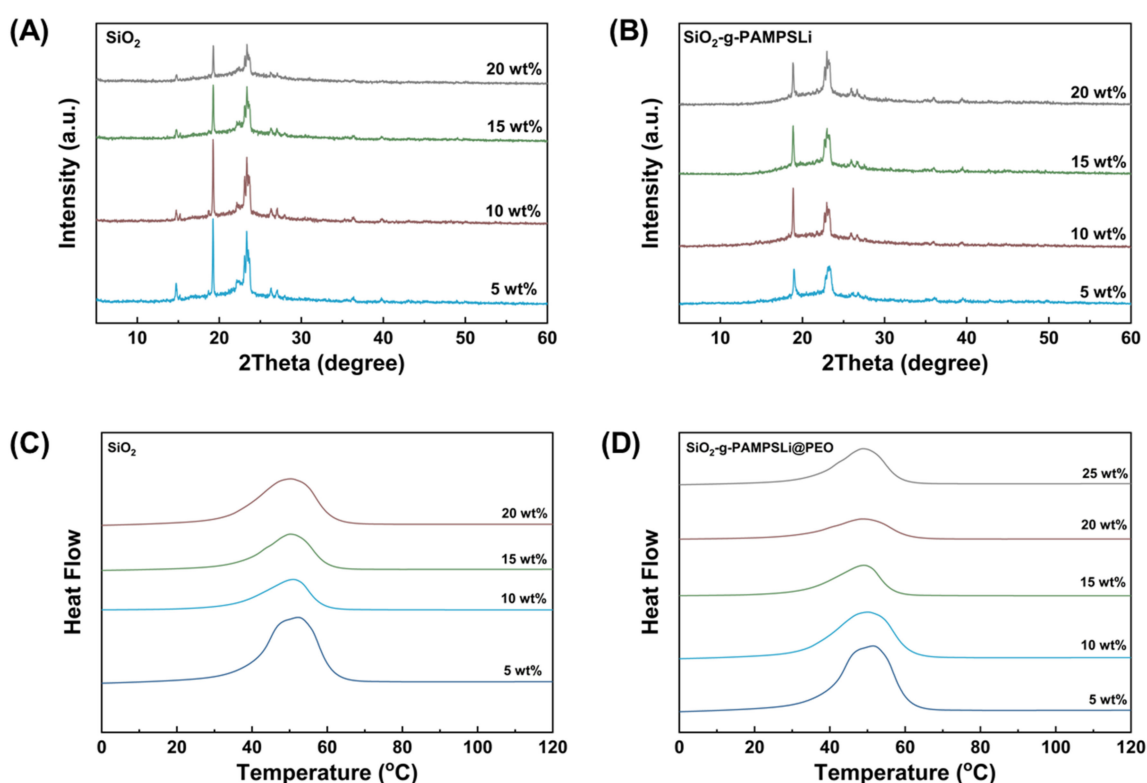


Figure 3. The XRD spectra and DSC curves of SPEs containing varying amounts of (A,C) SiO₂ and (B,D) SiO₂-g-PAMPSLi.

Here, χ_c represents the crystallinity of polymer PEO, and ΔH_{PEO} denotes the enthalpy of fusion for fully crystallized PEO, with a value of 196.4 J g^{-1} . ΔH_m corresponds to the experimentally measured enthalpy of fusion, and f_{PEO} represents the mass fraction of PEO in the SPEs.

The XRD spectra of individual SiO₂ and SiO₂-g-PAMPSLi exhibited no distinct diffraction peaks, indicating their amorphous nature. In comparison to the XRD spectrum of SiO₂@PEO, the XRD spectrum of SiO₂-g-PAMPSLi@PEO did not exhibit the diffraction peaks at 14.9° and 22.3° . This suggests the presence of interactions between certain functional groups on SiO₂-g-PAMPSLi and the PEO chains, which may affect the crystallization behavior of PEO and disrupt the corresponding crystalline regions associated with these diffraction peaks. With an increase in the loading of SiO₂-g-PAMPSLi, the intensity of the characteristic diffraction peaks of PEO at 19.2° and 23.5° decreased, indicating the ability of SiO₂-g-PAMPSLi to reduce the crystallinity of PEO. The DSC curves reveal that although the melting temperature of SiO₂-g-PAMPSLi@PEO shows a slight increase with increas-

ing SiO₂-g-PAMPSLi content, the intensity of the melting peak significantly decreases. This observation is consistent with the results of melting temperature and crystallinity presented in Table S1. As shown in Table S1, when the SiO₂-g-PAMPSLi content is below 20 wt%, the crystallinity of SiO₂-g-PAMPSLi@PEO notably decreases with increasing SiO₂-g-PAMPSLi content, reaching a minimum value of 24% at 20 wt%. Nevertheless, when the SiO₂-g-PAMPSLi content exceeds a certain threshold, particle aggregation occurs (Figure S3), resulting in reduced interaction with polymer PEO and increased crystallinity. Furthermore, compared to SiO₂@PEO, SiO₂-g-PAMPSLi@PEO exhibits lower crystallinity at the same filler content, and the difference becomes more pronounced as the filler content increases. This phenomenon can be attributed to the presence of abundant amine and unreacted hydroxyl groups on the surface of SiO₂-g-PAMPSLi particles. The hydrogen atoms on these functional groups can form stronger hydrogen bonds with the ether oxygen atoms in PEO, surpassing the hydrogen bonding effect of the hydroxyl groups on SiO₂. As a result, the impact on PEO crystallization is more pronounced, leading to a more effective reduction in PEO crystallinity. Additionally, the SiO₂-g-PAMPSLi@PEO system achieves the lowest crystallinity at a higher filler content compared to SiO₂@PEO. This is attributed to the excellent dispersion of SiO₂-g-PAMPSLi particles in PEO, even at higher contents, as confirmed by the SEM image in Figure S3.

To investigate the interaction mechanism between SiO₂-g-PAMPSLi particles and polymer PEO in SiO₂-g-PAMPSLi@PEO, the mechanical properties were evaluated through tensile testing, as shown in Figure S4. PEO and SiO₂@PEO with an equivalent filler content were selected as control groups. As observed from the graph, PEO exhibits a tensile strength of only 2.2 MPa and a fracture elongation of approximately 330% in the absence of filler addition. Upon the addition of nanoscale particle fillers, both SPE systems demonstrate a significant improvement in tensile strength and fracture elongation. This indicates that both types of nanoscale particles enhance and toughen the polymer PEO. Furthermore, SiO₂-g-PAMPSLi exhibits superior reinforcement and toughening effects on polymer PEO compared to SiO₂. This can be attributed to two factors: firstly, the surface of SiO₂-g-PAMPSLi contains a substantial number of functional groups capable of interacting with PEO chains, thereby enhancing the tensile strength of SPEs. Secondly, at an equivalent filler content, SiO₂-g-PAMPSLi@PEO exhibits lower crystallinity, leading to enhanced material toughness and increased fracture elongation. Figure S5 presents the stress–strain curves of SiO₂-g-PAMPSLi@PEO with different SiO₂-g-PAMPSLi contents. It can be observed that both the tensile strength and fracture elongation of SiO₂-g-PAMPSLi@PEO increase with an increase in SiO₂-g-PAMPSLi content. However, when the content reaches 25 wt%, the fracture elongation decreases. This behavior can be attributed to the stronger interaction between SiO₂-g-PAMPSLi and polymer PEO at higher SiO₂-g-PAMPSLi contents, leading to enhanced tensile strength and fracture elongation. Nevertheless, when the SiO₂-g-PAMPSLi content exceeds a certain threshold, particle aggregation occurs, resulting in reduced interaction with polymer PEO, increased crystallinity, and decreased flexibility. Consequently, the fracture elongation decreases.

The lithium-ion conductivity relationship with filler content at room temperature (25 °C) for SPEs is depicted in Figure 4A. It is evident that the lithium-ion conductivity of SiO₂-g-PAMPSLi@PEO consistently surpasses that of SiO₂@PEO at equivalent filler content. Moreover, as the filler content increases, the disparity between the two becomes more pronounced, reaching an order of magnitude higher lithium-ion conductivity for SiO₂-g-PAMPSLi@PEO compared to SiO₂@PEO at higher concentrations. On one hand, under equivalent content conditions, the crystallinity of SiO₂-g-PAMPSLi@PEO is lower than that of SiO₂@PEO, promoting an increase in the proportion of amorphous PEO molecular chains favorable for Li⁺ migration and transport, thereby enhancing lithium-ion conductivity. On the other hand, the surface of SiO₂-g-PAMPSLi particles is rich in lithium sulfonate groups, facilitating interaction with Li⁺ to promote salt dissociation and possessing inherent Li⁺ conductivity. Consequently, SPEs incorporating SiO₂-g-PAMPSLi exhibit significantly improved lithium-ion conductivity. However, when the SiO₂-g-PAMPSLi content exceeds a

certain threshold, the lithium-ion conductivity of SiO₂-g-PAMPSLi@PEO decreases. This is attributed to the agglomeration of SiO₂-g-PAMPSLi particles at higher concentrations, increasing the crystallinity of SiO₂-g-PAMPSLi@PEO and consequently leading to a reduction in lithium-ion conductivity.

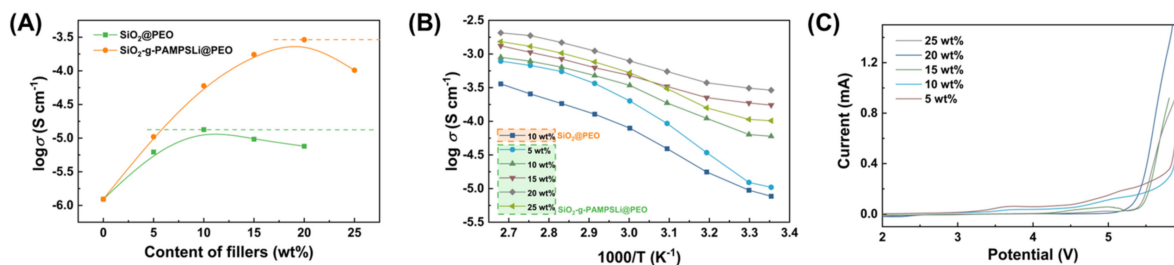


Figure 4. The relationship between lithium-ion conductivity of various SPEs and (A) filler loading levels, as well as (B) temperature; (C) Linear sweep voltammetry tests of SiO₂-g-PAMPSLi@PEO composites with varying SiO₂-g-PAMPSLi content.

Temperature experiments on the lithium-ion conductivity of SiO₂-g-PAMPSLi@PEO with varying SiO₂-g-PAMPSLi content were conducted, using 10 wt% SiO₂@PEO as a control group (Figure 4B). The results demonstrate that the lithium-ion conductivity of all SPEs increases with temperature elevation, particularly in the range of 40 °C to 70 °C. This is attributed to the transition of crystalline PEO chains to a molten state from 40 °C, enhancing the free movement of PEO chains and facilitating Li⁺ migration and transport, resulting in a noticeable increase in solid electrolyte lithium-ion conductivity. Beyond 80 °C, PEO enters a fully molten state, and the lithium-ion conductivity of solid electrolytes conforms to the Vogel–Tamman–Fulcher equation with temperature variations [31].

Figure S5 presents the chronoamperometric curves and corresponding pre- and post-polarization AC impedance spectra at room temperature (25 °C) for SiO₂-g-PAMPSLi@PEO with varying SiO₂-g-PAMPSLi content, with the summarized test results provided in Table S3. It is observed that the lithium-ion transference number of SiO₂-g-PAMPSLi@PEO increases with higher SiO₂-g-PAMPSLi content. This enhancement can be attributed to the presence of the polymer PAMPSLi layer on the surface of SiO₂-g-PAMPSLi particles, which not only facilitates Li⁺ migration and transport but also interacts with PEO molecular chains, reducing the crystallinity of PEO and promoting Li⁺ migration and transport.

Linear sweep voltammetry tests were conducted on SiO₂-g-PAMPSLi@PEO composites with varying SiO₂-g-PAMPSLi content, as depicted in Figure 4C. It is evident from the graph that with increasing SiO₂-g-PAMPSLi content, the electrochemical stability window of SiO₂-g-PAMPSLi@PEO also rises. Notably, all SiO₂-g-PAMPSLi@PEO composites exhibit electrochemical stability windows exceeding 5.0 V (vs. Li/Li⁺), meeting the electrolyte requirements of Li-S batteries. Following a series of electrochemical performance assessments, it was determined that the electrochemical performance of the 20 wt% SiO₂-g-PAMPSLi@PEO composite was optimal. Consequently, the 20 wt% SiO₂-g-PAMPSLi@PEO composite was selected as the solid electrolyte for assembling solid-state Li-S batteries, which were subsequently subjected to further battery performance evaluations.

Figure 5A illustrates the cyclic voltammetry curves of Li-S batteries employing SiO₂-g-PAMPSLi@PEO as SPEs. The curves exhibit two distinct reduction peaks and one oxidation peak, indicative of the typical multi-step reaction mechanism in Li-S batteries. The higher reduction peak at 2.30 V corresponds to the reduction of elemental sulfur (S₈) to long-chain polysulfides Li₂S_x (4 ≤ x ≤ 8), while the lower reduction peak at 2.00 V corresponds to the further reduction of long-chain polysulfides to short-chain sulfides Li₂S₂ and Li₂S. Correspondingly, the oxidation peak at 2.43 V corresponds to the reverse oxidation reaction from short-chain sulfides Li₂S₂ and Li₂S to long-chain polysulfides Li₂S_x.

($4 \leq x \leq 8$) and ultimately to elemental sulfur (S_8). During the initial three cycles, the cyclic voltammetry curves overlap closely, with no significant shifts in the oxidation-reduction peaks, indicating excellent cycle reversibility and stability of Li-S batteries utilizing SiO_2 -g-PAMPSLi@PEO. The constant current charge–discharge profiles at standard temperature ($25\text{ }^\circ\text{C}$) and 0.1 C current rate conditions of Li-S batteries employing SiO_2 -g-PAMPSLi@PEO as SPEs (Figure 5B) reveal a continuous charging plateau ($\sim 2.20\text{ V}$) and two discharging plateaus ($\sim 2.35\text{ V}$ and $\sim 2.10\text{ V}$), representing the oxidation reaction from Li_2S to elemental sulfur S_8 and the two-step reduction reaction from elemental sulfur S_8 to polysulfides Li_2S_x ($4 \leq x \leq 8$) and then to Li_2S . These steps correspond to the oxidation peak and two reduction peaks observed in the cyclic voltammetry curve, demonstrating that the oxidation-reduction reactions occurring during the charge–discharge cycles of the SiO_2 -g-PAMPSLi@PEO Li-S battery are characteristic of typical electrochemical redox reactions in Li-S batteries. Furthermore, Li-S batteries utilizing SiO_2 -g-PAMPSLi@PEO as SPEs demonstrate outstanding rate capabilities (Figure 5C). As the current rate escalates from 0.1 C to 1 C , the discharge-specific capacities of the Li-S batteries are recorded as 1098.3 mAh g^{-1} , 966.3 mAh g^{-1} , 777.5 mAh g^{-1} , 419.4 mAh g^{-1} , and 189.2 mAh g^{-1} . Upon reverting back to 0.1 C , the discharge-specific capacity of the batteries can recover to approximately 987.3 mAh g^{-1} , underscoring the exceptional reversibility of the Li-S system. Illustrated in Figure 5D are the constant current charge–discharge profiles of Li-S batteries employing SiO_2 -g-PAMPSLi@PEO as SPEs under current rates ranging from 0.1 C to 1 C . The congruence in the shapes of all curves within the graph indicates that the Li-S battery undergoes the same electrochemical reactions at different current rates, devoid of any side reactions.

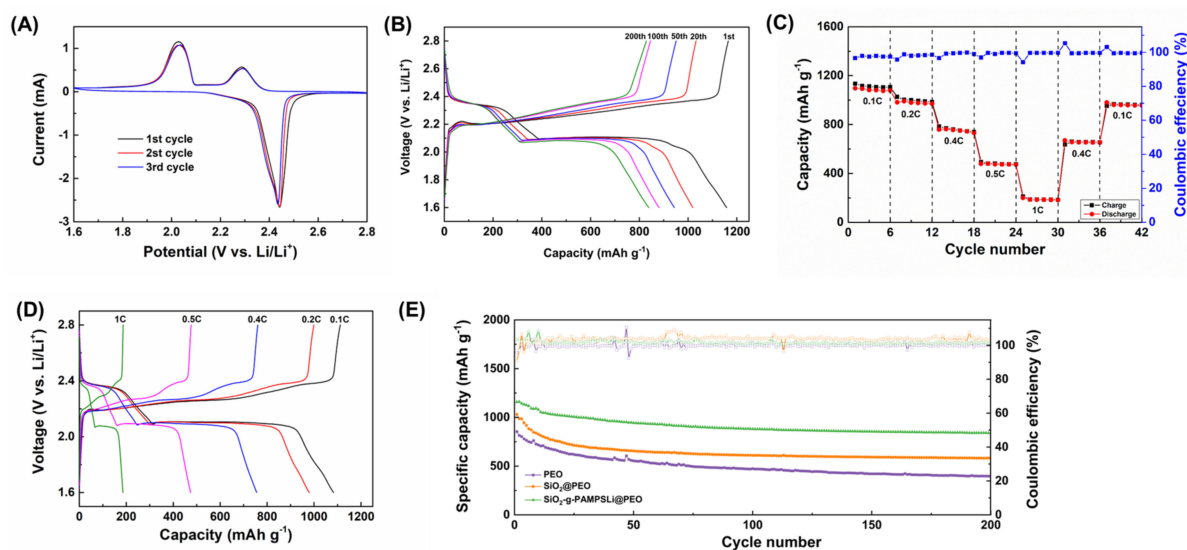


Figure 5. (A) Cyclic voltammetry curves of Li-S batteries employing SiO_2 -g-PAMPSLi@PEO as SPEs; (B) constant current charge–discharge profiles of Li-S batteries utilizing SiO_2 -g-PAMPSLi@PEO as SPEs under standard temperature ($25\text{ }^\circ\text{C}$) and 0.1 C current rate conditions are also depicted; (C) rate performance and (D) charge–discharge profiles at current densities ranging from 0.1 C to 1 C of Li-S batteries employing SiO_2 -g-PAMPSLi@PEO as SPEs; (E) discharge capacities and Coulombic efficiencies of Li-S batteries employing PEO, SiO_2 @PEO, and SiO_2 -g-PAMPSLi@PEO as SPEs under standard temperature ($25\text{ }^\circ\text{C}$) and 0.1 C current rate conditions.

By employing constant current charge–discharge methodology under standard temperature ($25\text{ }^\circ\text{C}$) and at a 0.1 C current rate, the electrochemical performance of Li-S batteries utilizing @PEO as SPEs was assessed, as depicted in Figure 5E, with PEO and SiO_2 @PEO serving as control groups. Upon examination, the initial discharge-specific capacities of the three types of Li-S batteries using PEO, SiO_2 @PEO, and SiO_2 -g-PAMPSLi@PEO as SPEs were recorded as 854.5 mAh g^{-1} , 1030.5 mAh g^{-1} , and 1211.4 mAh g^{-1} , respectively. Following 200 cycles, the discharge-specific capacities of these batteries stood at

395.8 mAh g⁻¹, 581.2 mAh g⁻¹, and 875.2 mAh g⁻¹, respectively. Evidently, the cyclic performance of the Li-S battery employing SiO₂-g-PAMPSLi@PEO surpassed that of the other two variants, maintaining a Coulombic efficiency of approximately 100%. This enhancement can be attributed to the superior lithium-ion conductivity of SiO₂-g-PAMPSLi@PEO, facilitating more thorough electrochemical reactions. Additionally, the favorable compatibility between SiO₂-g-PAMPSLi and the polymer PEO enhances the contact performance between the composite solid electrolyte and the electrodes, optimizing discharge capacity.

4. Conclusions

To mitigate the inert nature of SiO₂ Nps, their tendency for aggregation, and their inadequate inorganic–organic compatibility with the polymer PEO, we employed an ARGET-ATRP approach involving the grafting of sulfonic acid-functionalized organic polymer chains onto SiO₂ Nps. This strategic modification was pursued to confer Li⁺ conductivity characteristics to SiO₂ Nps and improve their compatibility with PEO. Subsequently, the modified nano fillers were blended with PEO using a solution-based method to fabricate SPE films. This approach ultimately led to the development of a polymer composite solid electrolyte. Experimental results demonstrate that this electrolyte manifests reduced crystallinity and exceptional Li⁺ conductivity, thereby displaying remarkable electrochemical performance during charge–discharge cycling in solid-state Li-S batteries.

Supplementary Materials: The following supporting information can be downloaded at: <https://www.mdpi.com/article/10.3390/polym16081128/s1>, Figure S1. The 1H NMR spectrum of pre-initiator. Figure S2. SEM images of (A) SiO₂ Nps and (B) SiO₂ Nps initiator. Figure S3. SEM images of SPEs with varying levels of (A–D) SiO₂ and (E–I) SiO₂-g-PAMPSLi content. Figure S4. The stress–strain curves of different SPEs. Figure S5. The stress–strain curves of SPEs with varying levels of SiO₂-g-PAMPSLi content. Table S1. DSC results of SPEs containing varying amounts of SiO₂. Table S2. DSC results of SPEs containing varying amounts of SiO₂-g-PAMPSLi. Figure S6. The chronoamperometric curves at room temperature (25 °C) and the corresponding pre- and post-polarization AC impedance spectra of the SPEs with varying levels of SiO₂-g-PAMPSLi content. Table S3. Li⁺ migration number of SPEs containing varying amounts of SiO₂-g-PAMPSLi. Table S4. The electrochemical performances of lithium–sulfur batteries with PEO-based SPEs. References [50–58] are cited in the supplementary materials.

Author Contributions: Idea of experiment, L.W. and W.R.; experiments, investigations, and analysis, L.W., J.H., Y.S., and M.M.; writing—original draft preparation, L.W.; writing—review and editing, L.W. and W.R.; validation and supervision, W.R. and M.Z. All authors have read and agreed to the published version of the manuscript.

Funding: This research was funded by the National Natural Science Foundation of China (grants number: 52033011 and 52173092) and the Guangxi Science and Technology Project (grant number: AB23049003).

Institutional Review Board Statement: Not applicable.

Data Availability Statement: Data are included in the article and Supplementary Materials. The data that support the findings of this study are available from the corresponding author, [W.R.], upon reasonable request.

Conflicts of Interest: The authors declare no conflict of interest.

References

1. Su, X.; Xu, X.-P.; Ji, Z.-Q.; Wu, J.; Ma, F.; Fan, L.-Z. Polyethylene Oxide-Based Composite Solid Electrolytes for Lithium Batteries: Current Progress, Low-Temperature and High-Voltage Limitations, and Prospects. *Electrochem. Energy Rev.* **2024**, *7*, 2–39. [[CrossRef](#)]
2. Chen, K.; Barai, P.; Kahvecioglu, O.; Wu, L.; Pupek, K.Z.; Ge, M.; Ma, L.; Ehrlich, S.N.; Zhong, H.; Zhu, Y.; et al. Cobalt-free composite-structured cathodes with lithium-stoichiometry control for sustainable lithium-ion batteries. *Nat. Commun.* **2024**, *15*, 430–439. [[CrossRef](#)] [[PubMed](#)]
3. Tao, Y.; Rahn, C.D.; Archer, L.A.; You, F. Second life and recycling: Energy and environmental sustainability perspectives for high-performance lithium-ion batteries. *Sci. Adv.* **2021**, *7*, eabi7633–eabi7648. [[CrossRef](#)] [[PubMed](#)]

4. Li, J.; Gao, L.; Pan, F.; Gong, C.; Sun, L.; Gao, H.; Zhang, J.; Zhao, Y.; Wang, G.; Liu, H. Engineering Strategies for Suppressing the Shuttle Effect in Lithium–Sulfur Batteries. *Nano-Micro Lett.* **2023**, *16*, 12–46. [[CrossRef](#)] [[PubMed](#)]
5. Qi, B.; Hong, X.; Jiang, Y.; Shi, J.; Zhang, M.; Yan, W.; Lai, C. A Review on Engineering Design for Enhancing Interfacial Contact in Solid-State Lithium–Sulfur Batteries. *Nano-Micro Lett.* **2024**, *16*, 71–104. [[CrossRef](#)]
6. Shaibani, M.; Mirshekarloo, M.S.; Singh, R.; Easton, C.D.; Cooray, M.C.D.; Eshraghi, N.; Abendroth, T.; Dörfler, S.; Althues, H.; Kaskel, S.; et al. Expansion-tolerant architectures for stable cycling of ultrahigh-loading sulfur cathodes in lithium-sulfur batteries. *Sci. Adv.* **2020**, *6*, eaay2757–eaay2766. [[CrossRef](#)]
7. Pei, F.; Wu, L.; Zhang, Y.; Liao, Y.; Kang, Q.; Han, Y.; Zhang, H.; Shen, Y.; Xu, H.; Li, Z.; et al. Interfacial self-healing polymer electrolytes for long-cycle solid-state lithium-sulfur batteries. *Nat. Commun.* **2024**, *15*, 351–360. [[CrossRef](#)] [[PubMed](#)]
8. Hong, X.; Liu, Y.; Li, Y.; Wang, X.; Fu, J.; Wang, X. Application Progress of Polyaniline, Polypyrrole and Polythiophene in Lithium-Sulfur Batteries. *Polymers* **2020**, *12*, 331. [[CrossRef](#)] [[PubMed](#)]
9. Yin, Y.-X.; Xin, S.; Guo, Y.-G.; Wan, L.-J. Lithium–Sulfur Batteries: Electrochemistry, Materials, and Prospects. *Angew. Chem. Int. Ed.* **2013**, *52*, 13186–13200. [[CrossRef](#)]
10. Wang, C.; Liu, R.; Liu, W.; Zhu, W.; Yang, X.; Wu, Q.; Xie, K.; Shen, L.; Wu, J.; Liu, Y.; et al. Porous Carbon Cloth@CoSe₂ as Kinetics-Enhanced and High-Loading Integrated Sulfur Host for Lithium–Sulfur Batteries. *Adv. Funct. Mater.* **2024**, 2316221–2316231. [[CrossRef](#)]
11. Wang, Z.; Song, C.; Shen, H.; Ma, S.; Li, G.; Li, Y. RuOx Quantum Dots Loaded on Graphdiyne for High-Performance Lithium–Sulfur Batteries. *Adv. Mater.* **2023**, *36*, 2307786–2307798. [[CrossRef](#)] [[PubMed](#)]
12. Wang, M.; Su, H.; Zhong, Y.; Hu, X.; Wang, X.; Gu, C.; Tu, J. Localized S-Li₂S Conversion with Accelerated Kinetics Mediated by Mixed Conductive Shell for High-Performance Solid-State Lithium-Sulfur Battery. *Adv. Energy Mater.* **2024**, *14*, 2302255. [[CrossRef](#)]
13. Mikhaylik, Y.V.; Akridge, J.R. Polysulfide Shuttle Study in the Li/S Battery System. *J. Electrochem. Soc.* **2004**, *151*, A1969–A1976. [[CrossRef](#)]
14. Yang, J.; Xiao, W.; Wu, X.; Zha, Y.; Liu, S. Preparation of GO/Diatomite/Polyacrylonitrile Functional Separator and Its Application in Li–S Batteries. *Materials* **2024**, *17*, 789. [[CrossRef](#)] [[PubMed](#)]
15. Talukder, N.; Wang, Y.; Nunna, B.B.; Lee, E.S. N-Doped Graphene (N-G)/MOF(ZIF-8)-Based/Derived Materials for Electrochemical Energy Applications: Synthesis, Characteristics, and Functionality. *Batteries* **2024**, *10*, 47. [[CrossRef](#)]
16. Zheng, Y.; Yao, Y.; Ou, J.; Li, M.; Luo, D.; Dou, H.; Li, Z.; Amine, K.; Yu, A.; Chen, Z. A review of composite solid-state electrolytes for lithium batteries: Fundamentals, key materials and advanced structures. *Chem. Soc. Rev.* **2020**, *49*, 8790–8839. [[CrossRef](#)] [[PubMed](#)]
17. Wang, J.; Liao, Y.; Wu, X.; Ye, L.; Wang, Z.; Wu, F.; Lin, Z. In Situ Construction of Elastic Solid-State Polymer Electrolyte with Fast Ionic Transport for Dendrite-Free Solid-State Lithium Metal Batteries. *Nanomaterials* **2024**, *14*, 433. [[CrossRef](#)] [[PubMed](#)]
18. Kumar, S.; Raghupathy, R.; Vittadello, M. Sodium Polymer Electrolytes: A Review. *Batteries* **2024**, *10*, 73. [[CrossRef](#)]
19. Patodia, T.; Gupta, M.K.; Singh, R.; Ichikawa, T.; Jain, A.; Tripathi, B. Electrochemical Performance of Graphene-Modulated Sulfur Composite Cathodes Using LiBH₄ Electrolyte for All-Solid-State Li-S Battery. *Energies* **2021**, *14*, 7362. [[CrossRef](#)]
20. Wang, L. Development of Novel High Li-Ion Conductivity Hybrid Electrolytes of Li₁₀GeP₂S₁₂ (LGPS) and Li_{6,6}La₃Zr_{1,6}Sb_{0,4}O₁₂ (LLZSO) for Advanced All-Solid-State Batteries. *Oxygen* **2021**, *1*, 16–21. [[CrossRef](#)]
21. Li, S.; Zhang, W.; Zheng, J.; Lv, M.; Song, H.; Du, L. Inhibition of Polysulfide Shuttles in Li–S Batteries: Modified Separators and Solid-State Electrolytes. *Adv. Energy Mater.* **2021**, *11*, 2000779–2000802. [[CrossRef](#)]
22. Zhang, J.; Chou, J.; Luo, X.-X.; Yang, Y.-M.; Yan, M.-Y.; Jia, D.; Zhang, C.-H.; Wang, Y.-H.; Wang, W.-P.; Tan, S.-J.; et al. A Fully Amorphous, Dynamic Cross-Linked Polymer Electrolyte for Lithium-Sulfur Batteries Operating at Subzero-Temperatures. *Angew. Chem. Int. Ed.* **2024**, 63–71, e202316087. [[CrossRef](#)]
23. Song, Z.; Jiang, W.; Li, B.; Qu, Y.; Mao, R.; Jian, X.; Hu, F. Advanced Polymers in Cathodes and Electrolytes for Lithium–Sulfur Batteries: Progress and Prospects. *Small* **2024**, 2308550. [[CrossRef](#)]
24. Wu, Z.-H.; Huang, A.-C.; Tang, Y.; Yang, Y.-P.; Liu, Y.-C.; Li, Z.-P.; Zhou, H.-L.; Huang, C.-F.; Xing, Z.-X.; Shu, C.-M.; et al. Thermal Effect and Mechanism Analysis of Flame-Retardant Modified Polymer Electrolyte for Lithium-Ion Battery. *Polymers* **2021**, *13*, 1675. [[CrossRef](#)]
25. Meyer, W.H. Polymer Electrolytes for Lithium-Ion Batteries. *Adv. Mater.* **1998**, *10*, 439–448. [[CrossRef](#)]
26. Song, Z.; Wang, L.; Jiang, W.; Pei, M.; Li, B.; Mao, R.; Liu, S.; Zhang, T.; Jian, X.; Hu, F. “Like Compatible Like” Strategy Designing Strong Cathode-Electrolyte Interface Quasi-Solid-State Lithium–Sulfur Batteries. *Adv. Energy Mater.* **2024**, *14*, 2302688–2302701. [[CrossRef](#)]
27. Feng, J.; Wang, L.; Chen, Y.; Wang, P.; Zhang, H.; He, X. PEO based polymer-ceramic hybrid solid electrolytes: A review. *Nano Converg.* **2021**, *8*, 2–13. [[CrossRef](#)]
28. Le Mong, A.; Shin, J.C.; Lee, M.; Kim, D. Accelerated Single Li-Ion Transport in Solid Electrolytes for Lithium–Sulfur Batteries: Poly(Arylene Ether Sulfone) Grafted with Pyrrolidinium-Terminated Poly(Ethylene Glycol). *Small* **2023**, 2309162. [[CrossRef](#)]
29. Chiu, L.-L.; Chung, S.-H. A Poly(ethylene oxide)/Lithium bis(trifluoromethanesulfonyl)imide-Coated Polypropylene Membrane for a High-Loading Lithium–Sulfur Battery. *Polymers* **2021**, *13*, 535. [[CrossRef](#)]
30. Babkova, T.; Kiefer, R.; Le, Q.B. Hybrid Electrolyte Based on PEO and Ionic Liquid with In Situ Produced and Dispersed Silica for Sustainable Solid-State Battery. *Sustainability* **2024**, *16*, 1683. [[CrossRef](#)]

31. Croce, F.; Appetecchi, G.B.; Persi, L.; Scrosati, B. Nanocomposite polymer electrolytes for lithium batteries. *Nature* **1998**, *394*, 456–458. [[CrossRef](#)]
32. Zhao, S.; Wu, Q.; Ma, W.; Yang, L. Polyethylene Oxide-Based Composites as Solid-State Polymer Electrolytes for Lithium Metal Batteries: A Mini Review. *Front. Chem.* **2020**, *8*, 4581–4601. [[CrossRef](#)] [[PubMed](#)]
33. Mao, G.; Saboungi, M.-L.; Price, D.L.; Armand, M.B.; Howells, W.S. Structure of Liquid PEO-LiTFSI Electrolyte. *Phys. Rev. Lett.* **2000**, *84*, 5536–5539. [[CrossRef](#)] [[PubMed](#)]
34. Song, J.Y.; Wang, Y.Y.; Wan, C.C. Review of gel-type polymer electrolytes for lithium-ion batteries. *J. Power Sources* **1999**, *77*, 183–197. [[CrossRef](#)]
35. Song, Z.; Chen, F.; Martinez-Ibañez, M.; Feng, W.; Forsyth, M.; Zhou, Z.; Armand, M.; Zhang, H. A reflection on polymer electrolytes for solid-state lithium metal batteries. *Nat. Commun.* **2023**, *14*, 4884–4896. [[CrossRef](#)] [[PubMed](#)]
36. Xue, Z.; He, D.; Xie, X. Poly(ethylene oxide)-based electrolytes for lithium-ion batteries. *J. Mater. Chem. A* **2015**, *3*, 19218–19253. [[CrossRef](#)]
37. Marmorstein, D.; Yu, T.H.; Striebel, K.A.; McLarnon, F.R.; Hou, J.; Cairns, E.J. Electrochemical performance of lithium/sulfur cells with three different polymer electrolytes. *J. Power Sources* **2000**, *89*, 219–226. [[CrossRef](#)]
38. Yang, Q.; Deng, N.; Zhao, Y.; Gao, L.; Cheng, B.; Kang, W. A review on 1D materials for all-solid-state lithium-ion batteries and all-solid-state lithium-sulfur batteries. *Chem. Eng. J.* **2023**, *451*, 138532–138549. [[CrossRef](#)]
39. Tian, W.; Li, Z.; Miao, L.; Sun, Z.; Wang, Q.; Jiao, L. Composite Quasi-Solid-State Electrolytes with Organic–Inorganic Interface Engineering for Fast Ion Transport in Dendrite-Free Sodium Metal Batteries. *Adv. Mater.* **2023**, *36*, 2308586. [[CrossRef](#)]
40. Guo, J.; Zheng, J.; Zhang, W.; Lu, Y. Recent Advances of Composite Solid-State Electrolytes for Lithium-Based Batteries. *Energy Fuels* **2021**, *35*, 11118–11140. [[CrossRef](#)]
41. Tambelli, C.C.; Bloise, A.C.; Rosário, A.V.; Pereira, E.C.; Magon, C.J.; Donoso, J.P. Characterisation of PEO–Al₂O₃ composite polymer electrolytes. *Electrochim. Acta* **2002**, *47*, 1677–1682. [[CrossRef](#)]
42. Zhao, W.; Su, Y.; Wen, X.; Wang, D. Manipulating crystallization behavior of poly(ethylene oxide) by functionalized nanoparticle inclusion. *Polymer* **2019**, *165*, 28–38. [[CrossRef](#)]
43. Jiang, S.; Yu, D.; Ji, X.; An, L.; Jiang, B. Confined crystallization behavior of PEO in silica networks. *Polymer* **2000**, *41*, 2041–2046. [[CrossRef](#)]
44. Li, Q.; Wang, X.; Wang, L.; Zhu, S.; Zhong, Q.; Li, Y.; Zhou, Q. Li⁺ Conduction in a Polymer/Li_{1.5}Al_{0.5}Ge_{1.5}(PO₄)₃ Solid Electrolyte and Li-Metal/Electrolyte Interface. *Molecules* **2023**, *28*, 8029. [[CrossRef](#)] [[PubMed](#)]
45. Shi, L.; Zhang, L.; Yang, Y.; Zhang, H.; Yao, R.; Yuan, C.; Cheng, S. In Situ Nano-SiO₂ Electrospun Polyethylene-Oxide-Based Nano-Fiber Composite Solid Polymer Electrolyte for High-Performance Lithium-Ion Batteries. *Nanomaterials* **2023**, *13*, 1294. [[CrossRef](#)] [[PubMed](#)]
46. Cui, J.; Zhou, Z.; Jia, M.; Chen, X.; Shi, C.; Zhao, N.; Guo, X. Solid Polymer Electrolytes with Flexible Framework of SiO₂ Nanofibers for Highly Safe Solid Lithium Batteries. *Polymers* **2020**, *12*, 1324. [[CrossRef](#)]
47. Zhou, T.H.; Ruan, W.H.; Rong, M.Z.; Zhang, M.Q.; Mai, Y.L. Keys to Toughening of Non-layered Nanoparticles/Polymer Composites. *Adv. Mater.* **2007**, *19*, 2667–2671. [[CrossRef](#)]
48. Stöber, W.; Fink, A.; Bohn, E. Controlled growth of monodisperse silica spheres in the micron size range. *J. Colloid Interface Sci.* **1968**, *26*, 62–69. [[CrossRef](#)]
49. Gucci, F.; Grasso, M.; Russo, S.; Leighton, G.J.T.; Shaw, C.; Brighton, J. Electrical and Mechanical Characterisation of Poly(ethylene)oxide–Polysulfone Blend for Composite Structural Lithium Batteries. *Polymers* **2023**, *15*, 2581. [[CrossRef](#)]
50. Eshetu, G.G.; Judez, X.; Li, C.; Martinez-Ibanez, M.; Gracia, I.; Bondarchuk, O.; Carrasco, J.; Rodriguez-Martinez, L.M.; Zhang, H.; Armand, M. Ultrahigh Performance All Solid-State Lithium Sulfur Batteries: Salt Anion’s Chemistry-Induced Anomalous Synergistic Effect. *J. Am. Chem. Soc.* **2018**, *140*, 9921–9933. [[CrossRef](#)]
51. Fang, R.; Xu, H.; Xu, B.; Li, X.; Li, Y.; Goodenough, J.B. Reaction Mechanism Optimization of Solid-State Li–S Batteries with a PEO-Based Electrolyte. *Adv. Funct. Mater.* **2020**, *31*, 2001812. [[CrossRef](#)]
52. Ji, Y.; Yang, K.; Liu, M.; Chen, S.; Liu, X.; Yang, B.; Wang, Z.; Huang, W.; Song, Z.; Xue, S.; et al. PIM-1 as a Multifunctional Framework to Enable High-Performance Solid-State Lithium–Sulfur Batteries. *Adv. Funct. Mater.* **2021**, *31*, 2104830. [[CrossRef](#)]
53. Gao, X.; Zheng, X.; Wang, J.; Zhang, Z.; Xiao, X.; Wan, J.; Ye, Y.; Chou, L.Y.; Lee, H.K.; Wang, J.; et al. Incorporating the Nanoscale Encapsulation Concept from Liquid Electrolytes into Solid-State Lithium–Sulfur Batteries. *Nano Lett.* **2020**, *20*, 5496–5503. [[CrossRef](#)] [[PubMed](#)]
54. Hong, S.; Wang, Y.; Kim, N.; Lee, S.B. Polymer-based electrolytes for all-solid-state lithium–sulfur batteries: From fundamental research to performance improvement. *J. Mater. Sci.* **2021**, *56*, 8358–8382. [[CrossRef](#)]
55. Li, M.; Frerichs, J.E.; Kolek, M.; Sun, W.; Zhou, D.; Huang, C.J.; Hwang, B.J.; Hansen, M.R.; Winter, M.; Bieker, P. Solid-State Lithium–Sulfur Battery Enabled by Thio-LiSICON/Polymer Composite Electrolyte and Sulfurized Polyacrylonitrile Cathode. *Adv. Funct. Mater.* **2020**, *30*, 1910123. [[CrossRef](#)]
56. Xu, X.; Hou, G.; Nie, X.; Ai, Q.; Liu, Y.; Feng, J.; Zhang, L.; Si, P.; Guo, S.; Ci, L. Li₇P₃S₁₁/poly(ethylene oxide) hybrid solid electrolytes with excellent interfacial compatibility for all-solid-state batteries. *J. Power Sources* **2018**, *400*, 212–217. [[CrossRef](#)]

57. Kou, W.; Wang, J.; Li, W.; Lv, R.; Peng, N.; Wu, W.; Wang, J. *Asymmetry-structure electrolyte with rapid Li⁺ transfer pathway towards high-performance all-solid-state lithium–sulfur battery*. *J. Membr. Sci.* **2021**, *634*, 119432. [[CrossRef](#)]
58. Liu, Y.; Liu, H.; Lin, Y.; Zhao, Y.; Yuan, H.; Su, Y.; Zhang, J.; Ren, S.; Fan, H.; Zhang, Y. *Mechanistic Investigation of Polymer-Based All-Solid-State Lithium/Sulfur Battery*. *Adv. Funct. Mater.* **2021**, *31*, 2104863. [[CrossRef](#)]

Disclaimer/Publisher’s Note: The statements, opinions and data contained in all publications are solely those of the individual author(s) and contributor(s) and not of MDPI and/or the editor(s). MDPI and/or the editor(s) disclaim responsibility for any injury to people or property resulting from any ideas, methods, instructions or products referred to in the content.